Interband optical transitions in left- and right-handed single-wall carbon nanotubes

doi: 10.1103/PhysRevB.69.205402

Interband optical transitions in left- and right-handed single-wall carbon nanotubes

Ge. G. Samsonidze,[1] A. Grüneis,[4] R. Saito,[4] A. Jorio,[5] A. G. Souza Filho,[6] G. Dresselhaus,[3] and M. S. Dresselhaus[1,2]
[1]*Department of Electrical Engineering and Computer Science, Massachusetts Institute of Technology, Cambridge, Massachusetts 02139-4307, USA*
[2]*Department of Physics, Massachusetts Institute of Technology, Cambridge, Massachusetts 02139-4307, USA*
[3]*Francis Bitter Magnet Laboratory, Massachusetts Institute of Technology, Cambridge, Massachusetts 02139-4307, USA*
[4]*Department of Physics, Tohoku University and CREST JST, Aoba, Sendai 980-8578, Japan*
[5]*Departamento de Física, Universidade Federal de Minas Gerais, Belo Horizonte, Minas Gerais 30123-970, Brazil*
[6]*Departamento de Física, Universidade Federal do Ceará, Fortaleza, Ceará 60455-900, Brazil*
(Received 11 November 2003; published 13 May 2004)

The nanotube handedness is defined for the complete determination of the nanotube atomic structure by its diameter and chirality. The interband electronic optical transition matrix elements are calculated and the dipole selection rules are derived for chiral carbon nanotubes and circularly polarized light propagating along the nanotube axis. The dipole selection rules are shown to depend on the nanotube handedness and on the helicity of the light, and this dependence is responsible for the optical activity of carbon nanotubes, when time-reversal symmetry is broken. The optical absorption spectra calculated for opposite light helicity or nanotube handedness show circular dichroism in chiral nanotubes. The optical activity of chiral nanotubes allows the nanotube handedness to be determined in optical experiments using circularly polarized light.

DOI: 10.1103/PhysRevB.69.205402 PACS number(s): 78.67.Ch, 78.40.−q, 78.30.Na, 78.20.Ek

I. INTRODUCTION

Light absorption and emission processes in single-wall carbon nanotubes (SWNTs) are governed by dipole selection rules[1,2] and by the depolarization effect.[1,3] While the depolarization effect implies that light polarized perpendicular to the tube axis is suppressed because of the much larger polarizability parallel to the tube axis, the dipole selection rules only allow electronic transitions between the valence and conduction bands within *the same* subband of index μ for light polarized along the tube axis. The depolarization effect is expected to be more pronounced for metallic SWNTs due to the presence of conduction electrons. If the light polarization vector is perpendicular to the SWNT axis, the dipole selection rules predict electronic transitions between two adjacent subbands[1,2,4] of indices μ and $\mu \pm 1$. The difference in the dipole selection rules for the parallel and perpendicular light polarization directions indicates different electronic transition energies, which in turn implies different resonance conditions. Thus, the interaction with light polarized perpendicular to the SWNT axis can be detected, in spite of the depolarization effect, by the proper selection of the resonance conditions, i.e., wavelength of light resonant with $\mu \rightarrow \mu \pm 1$ rather than with $\mu \rightarrow \mu$ transitions in a given SWNT. Resonance Raman spectroscopy (RRS) studies on isolated SWNTs confirm the predicted optical selection rules when changing the light polarization vector.[5]

The majority of optical experiments on isolated SWNTs are performed in the geometry where the SWNTs lie on a substrate (xz) and the laser beam propagates normal to the substrate (y), and thus normal to the SWNT axis (z), allowing one to change the direction of the light polarization vector with respect to the SWNT axis from parallel (z) to perpendicular (x). However, it is also possible to design the geometry of the experiment, such that the laser beam propagates along the SWNT axis (z). This can be achieved by using fibers of aligned SWNTs (Ref. 6) or growing aligned SWNTs by chemical vapor deposition in an electric field.[7] The light propagating along the SWNT axis (z) can be polarized perpendicular to the SWNT axis (x or y). While both optical electronic transitions $\mu \rightarrow \mu - 1$ and $\mu \rightarrow \mu + 1$ are symmetry allowed for linearly polarized light (x or y), only one of these two transitions survives in the case of circularly polarized light ($x \pm iy$), depending on the SWNT handedness and on the light helicity. The left ($\mathrm{L} = x + iy$) and right ($\mathrm{R} = x - iy$) helicity of the light corresponds to left-handed or right-handed rotation of the polarization vector when looking along the direction of propagation (z), respectively.[8] The SWNT handedness is defined as AL or AR, depending on the rotation of two of the three armchair (A) chains of the carbon atoms to the L or to the R, when looking along the SWNT axis (z). While the absorption of the L circularly polarized light induces the electronic transitions $\mu \rightarrow \mu + 1$ for AL handed SWNTs and $\mu \rightarrow \mu - 1$ for AR handed SWNTs, the absorption of the R circularly polarized light induces the transitions $\mu \rightarrow \mu - 1$ for AL handed SWNTs and $\mu \rightarrow \mu + 1$ for AR handed SWNTs. The difference in the dipole selection rules for L and R circularly polarized light gives rise to optical activity (circular dichroism and circular birefringence) of chiral SWNTs.[9,10] The difference in the dipole selection rules for AL and AR handed SWNTs provides a way to identify SWNT handedness in optical experiments with circularly polarized light. Alternatively, the SWNT chirality, and thus also the SWNT handedness, can be determined from images of individual SWNTs taken by scanning tunneling microscopy (Ref. 11) and TEM (Ref. 12) techniques.

In the present paper we demonstrate the possibility to determine SWNT handedness by optical spectroscopy. The paper is organized as follows. An extended definition of SWNT

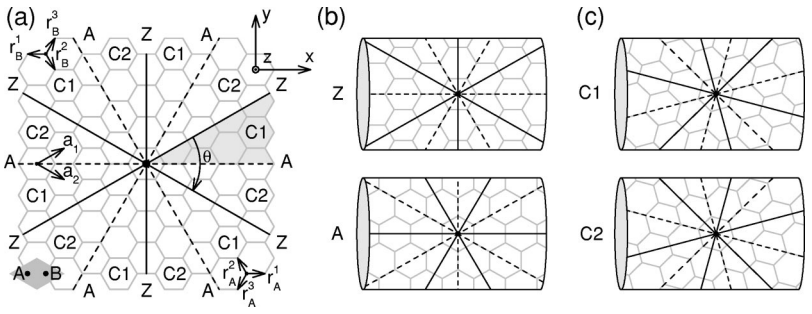

FIG. 1. (a) The graphene layer broken into 30° sectors where the chiral vector of the SWNT can be defined. Solid and dashed lines, labeled by Z and A, respectively, stand for zigzag and armchair achiral SWNTs, while the C1 and C2 sectors represent chiral SWNTs of opposite handedness. (b) Z and A achiral SWNTs. (c) C1 and C2 chiral SWNTs, obtained from the graphene layer in (a), by rolling from the front to the back.

chirality and SWNT handedness is introduced in Sec. II. The optical selection rules for circularly polarized light are derived from the electronic dipole transition matrix elements in Sec. III. While the same selection rules can be obtained by symmetry considerations using group theory, as discussed in Sec. IV, the matrix elements calculated in Sec. III are essential for the quantitative analysis of the optical absorption spectra of chiral SWNTs regarding their handedness and light helicity, as presented in Sec. IV. Concluding remarks follow in Sec. V.

II. NANOTUBE HANDEDNESS

A SWNT can be considered as a graphene layer rolled up into a seamless cylinder. The nanotube structure is uniquely determined by the chiral vector $\mathbf{C}_h$ in the graphene layer which spans the circumference of the SWNT.[13] The chiral vector consists of integral numbers of the unit vectors $\mathbf{a}_1$ and $\mathbf{a}_2$ shown in Fig. 1(a), $\mathbf{C}_h = n\mathbf{a}_1 + m\mathbf{a}_2$. The chiral vector is thus uniquely defined by a pair of integer numbers (n,m). Alternatively, the chiral vector can be defined by its length $C_h = \pi d_t$, where d_t is the tube diameter, and by its angle θ to one of the zigzag directions in the graphene layer, labeled by Z in Fig. 1(a). The chiral angle θ takes values 0 and $\pi/6$ for zigzag and armchair achiral SWNTs, when the chiral vector $\mathbf{C}_h$ is aligned along the Z and A directions in the graphene layer, respectively [see Fig. 1(a)].[14] Values of the chiral angle θ between 0 and $\pi/6$ correspond to chiral SWNTs, when the chiral vector is defined within the gray colored sector in the graphene layer in Fig. 1(a).

The chiral vector can be defined within one of twelve 30° sectors in the graphene layer shown in Fig. 1(a). While the gray colored sector and the five equivalent sectors labeled by C1 in Fig. 1(a) correspond to SWNTs of a given handedness, the six C2 sectors, which are also equivalent between themselves, yield SWNTs of the opposite handedness. The SWNTs of opposite handedness are related to each other by the one-dimensional (1D) spatial inversion along the SWNT axis. The SWNT handedness is also determined by the type of rolling of the graphene layer, either from the front of the layer to the back, or from the back to the front, as defined in Ref. 9, so that the printed side of Fig. 1(a) becomes, respectively, either the outer or the inner surface of the cylinder. By specifying the type of rolling from the front to the back, we can define SWNTs of both handedness by varying the chiral angle in the range from 0 to $\pi/3$ over the two rightmost 30° sectors in Fig. 1(a), C1 and C2. Here, the values of the chiral angle $\theta = 0$, $0 < \theta < \pi/6$, $\theta = \pi/6$, and $\pi/6 < \theta < \pi/3$ correspond to Z, C1, A, and C2 SWNTs, respectively. In terms of the (n,m) indices, Z, C1, A, and C2 SWNTs correspond to $m = 0$, $0 < m < n$, $m = n$, and $0 < n < m$, respectively. In other words, C1 and C2 SWNTs are related to each other by interchanging their n and m indices, i.e., the two pairs of indices (n,m) and (m,n) correspond to two SWNTs of the same diameter d_t and the same chiral angle θ defined in the range $0 < \theta < \pi/6$ but of opposite handedness. The two pairs of indices become (n,m) and $(n+m,-m)$ by selecting the upper-right C2 sector instead of the rightmost in Fig. 1(a).[12]

Z and A achiral SWNTs are shown in Fig. 1(b), and C1 and C2 chiral SWNTs in Fig. 1(c). While L- and R-handed organic molecules are commonly defined according to the direction of rotation of the atomic chain when looking along the molecular axis, the L or R handedness of C1 and C2 chiral SWNTs is not so obvious. There are three A directions and three Z directions in the graphene layer, as shown in Fig. 1(a). In the case of a C1 chiral SWNT [see Fig. 1(c)], two of the three A lines are rotated to the left and the third A line to the right when looking along the SWNT axis. At the same time, two of the three Z lines are rotated to the right and the third Z line to the left when looking along the SWNT axis. We thus can refer to C1 chiral SWNTs either as armchair left-handed (AL) tubes or as zigzag right-handed (ZR) tubes. Similarly, C2 chiral SWNTs can be referred to either as AR or as ZL. Note that while chiral SWNTs can be either of AL or of AR handedness, zigzag and armchair achiral SWNTs have no explicit handedness associated with them. This implies that there are twice as many chiral SWNTs for each pair of (n,m) indices as achiral SWNTs, once the indices are defined in the range $0 \leqslant m \leqslant n$. This aspect must be taken into account when analyzing the distribution of the (n,m) indices in a SWNT sample.

III. INTERBAND OPTICAL TRANSITIONS

The optical dipole transitions in graphite and in SWNTs have been recently studied regarding the electronic wave-vector dependence of their optical transition matrix elements.[4,15,16] In the present section, we focus on the photon wave-vector and polarization dependence of the matrix elements, which guides us to the optical activity of chiral SWNTs through the optical selection rules for circularly polarized light.

The interband electronic optical transition matrix element for SWNTs is given by

$$M^{\rho}_{\mathrm{opt}} = \langle \Psi_f | H^{\rho}_{\mathrm{opt}} | \Psi_i \rangle, \tag{1}$$

where Ψ_ι and Ψ_f are the wave functions of the initial (ι) and final (f) electronic states in the valence (v) and conduction (c) bands, and $H^\rho_{\rm opt}$ is the optical perturbation Hamiltonian for the absorbed ($\rho=a$) or emitted ($\rho=e$) light, expressed, to first order, by

$$H^\rho_{\rm opt} \cong i\frac{e\hbar}{mc}\mathbf{A}_\rho\cdot\boldsymbol{\nabla} \tag{2}$$

with the vector potential of the electromagnetic wave given by

$$\mathbf{A}_\rho=\frac{1}{\omega_\rho}\sqrt{\frac{cI_\rho}{\epsilon}}e^{\Upsilon i(\boldsymbol{\kappa}_\rho\cdot\mathbf{r}-\omega_\rho t)}\mathbf{P}_\rho . \tag{3}$$

Here, ω_ρ, $\boldsymbol{\kappa}_\rho$, $\mathbf{P}_\rho$, and I_ρ denote photon frequency, photon wave vector, photon polarization, and light intensity, respectively, for the absorbed ($\rho=a,\iota=v,f=c$) or emitted ($\rho=e,\iota=c,f=v$) light. The factor Υ reflects the time dependence of the optical field for the absorption ($\rho=a,\Upsilon=+1$) or emission ($\rho=e,\Upsilon=-1$) of light. The wave vector of the emitted photon is $\boldsymbol{\kappa}_e\simeq\mp\boldsymbol{\kappa}_a$ for the backscattering and transmission geometries, respectively. Within the dipole approximation, the photon wave vector $\boldsymbol{\kappa}_\rho$ is neglected in comparison to the electronic wave vectors $\mathbf{k}_\iota$ and $\mathbf{k}_f$. By substituting Eq. (3) into Eq. (2) and then Eq. (2) into Eq. (1), the electronic optical transition matrix element becomes

$$M^\rho_{\rm opt}=i\frac{e\hbar}{m\omega_\rho}\sqrt{\frac{I_\rho}{\epsilon c}}e^{i(\omega_f-\omega_\iota-\Upsilon\omega_\rho)t}\mathbf{P}_\rho\cdot\mathbf{D}, \tag{4}$$

where $\omega_J=E_J/\hbar$ in which E_J is the energy of the initial ($J=\iota$) or final ($J=f$) electronic state, and $\mathbf{D}$ is the dipole vector defined by

$$\mathbf{D}=\langle\Psi_f|\boldsymbol{\nabla}|\Psi_\iota\rangle. \tag{5}$$

To obtain the matrix element of Eq. (4) we thus need to calculate the dipole vector of Eq. (5), which requires knowledge of the electronic wave functions Ψ_J ($J=\iota,f$ or $J=v,c$). To construct the electronic wave functions, we first define the geometrical structure of the SWNT.

The unit cell of the graphene layer is a rhombus bounded by the unit vectors $\mathbf{a}_1$ and $\mathbf{a}_2$. Each rhombus consists of two inequivalent atomic sites, A and B [see Fig. 1(a)]. The graphene unit cells can be equally represented by the hexagons of the honeycomb lattice. Yet visually more convenient, each hexagon contains six carbon atoms and each carbon atom sits among three hexagons opening multiple ways to define the unit cell of hexagonal shape. In what follows, we refer to the unit cells of the graphene layer as hexagons for convenience, but we imply rhombi rather than hexagons when writing the coordinates of the atomic sites to avoid multiple interpretations.

The nanotube unit cell is a cylindrical segment of length $T=|\mathbf{T}|$, where $\mathbf{T}$ is the nanotube translation vector.[13] The number of nanotube unit cells $U=L/T$ is determined by the nanotube length L. The unrolled nanotube unit cell is given by a rectangle on the graphene layer bounded by the vectors $\mathbf{C}_h$ and $\mathbf{T}$. This rectangle consists of N hexagons, where $N=2(n^2+nm+m^2)/d_R$ and d_R is the greatest common divisor of $(2n+m)$ and $(2m+n)$ for the (n,m) SWNT.[13] In what follows, we refer to the coordinates of the atomic sites of the unrolled SWNT by $\mathbf{R}^u_{hs}$, where $u=1,\ldots,U$ denotes the nanotube unit cells, $h=1,\ldots,N$ denotes the hexagons within the nanotube unit cell, and $s=A,B$ denotes the atomic sites within the hexagon.

The electronic wave function Ψ_J ($J=\iota,f$ or $J=v,c$) can be written as a sum over the Bloch functions Φ_s ($s=A,B$) for A and B carbon atoms within the hexagon,

$$\Psi_J(\mathbf{r},\mathbf{k}_J)=\sum_{s=A}^{B}C^J_s(\mathbf{k}_J)\Phi_s(\mathbf{r},\mathbf{k}_J). \tag{6}$$

In the tight-binding approximation, the Bloch functions Φ_s ($s=A,B$) are expressed by the linear combinations of atomic $2p_z$ orbitals $\phi(\mathbf{r}-\mathbf{R}^u_{hs})$,

$$\Phi_s(\mathbf{r},\mathbf{k}_J)=\frac{1}{\sqrt{U}}\sum_{u=1}^{U}\ \frac{1}{\sqrt{N}}\sum_{h=1}^{N}e^{i\mathbf{k}_J\cdot\mathbf{R}^u_{hs}}\phi(\mathbf{r}-\mathbf{R}^u_{hs}). \tag{7}$$

The limitations of the tight-binding approximation will be discussed in Sec. IV. Note that the sum over index h (over the N hexagons in the SWNT unit cell) must be formally placed in the wave function of Eq. (6). We place this sum in the Bloch function of Eq. (7) instead, or in other words, we sum the Bloch functions over the N hexagons in the SWNT unit cell, within the framework of the zone-folding approach.[13] We are allowed to do so because of the equivalence of the N hexagons in the nanotube unit cell, which implies that the wave-function coefficients C^J_s in Eq. (6) are independent of the hexagon index h.

We now substitute the wave functions given by Eqs. (6) and (7) into the dipole vector of Eq. (5). This yields a sum of the dipole matrix elements between different atomic orbitals $\langle\phi(\mathbf{r}-\mathbf{R}^{u'}_{h's'})|\boldsymbol{\nabla}|\phi(\mathbf{r}-\mathbf{R}^u_{hs})\rangle$ with different phase factors and wave-function coefficients $C^{f*}_{s'}C^\iota_s$. Because of the rather fast decay of the atomic orbitals $\phi(\mathbf{r})$ away from the nuclei, we can limit our consideration to the nearest-neighbor dipole matrix elements. The resulting dipole vector can then be written in the form[4]

$$\begin{aligned}\mathbf{D}=\frac{\sqrt{3}M_{\rm dip}}{aNU}\Bigg[&C^{f*}_BC^\iota_A\sum_{u=1}^{U}\sum_{h=1}^{N}e^{i(\mathbf{k}_\iota-\mathbf{k}_f)\cdot\mathbf{R}^u_{hA}}\\&\times\sum_{\ell=1}^{3}e^{-i\mathbf{k}_f\cdot\mathbf{r}^\ell_A}\Omega\mathbf{r}^\ell_A\\&+C^{f*}_AC^\iota_B\sum_{u=1}^{U}\sum_{h=1}^{N}e^{i(\mathbf{k}_\iota-\mathbf{k}_f)\cdot\mathbf{R}^u_{hB}}\sum_{\ell=1}^{3}e^{-i\mathbf{k}_f\cdot\mathbf{r}^\ell_B}\Omega\mathbf{r}^\ell_B\Bigg],\end{aligned} \tag{8}$$

where $\mathbf{r}^\ell_A=\mathbf{R}^{u_\ell}_{h_\ell B}-\mathbf{R}^u_{hA}$ and $\mathbf{r}^\ell_B=\mathbf{R}^{u_\ell}_{h_\ell A}-\mathbf{R}^u_{hB}$ are the vectors pointing to the nearest-neighbor carbon atoms starting from the central A atom and from the central B atom, respectively, numbered by the index $\ell=1,\ldots,3$. The nearest-neighbor vectors $\mathbf{r}^\ell_s$ ($s=A,B$ and $\ell=1,\ldots,3$) are shown in Fig. 1(a),

where we set $\mathbf{r}_B^\ell = -\mathbf{r}_A^\ell$. The factor $M_{\rm dip}$ in Eq. (8) is the dipole matrix element between the two nearest-neighbor carbon atoms defined by

$$\langle \phi(\mathbf{r}-\tfrac{1}{2}\mathbf{r}_s^\ell)|\nabla|\phi(\mathbf{r}+\tfrac{1}{2}\mathbf{r}_s^\ell)\rangle = \frac{\sqrt{3}M_{\rm dip}\mathbf{r}_s^\ell}{a}, \tag{9}$$

where $a=0.246$ nm is the lattice constant of the graphene layer and $|\mathbf{r}_s^\ell| = a/\sqrt{3} = a_{\text{C-C}} = 0.142$ nm is the interatomic C-C distance in the graphene layer.

The operator Ω in Eq. (8) places the nearest-neighbor vectors $\mathbf{r}_s^\ell$ on the cylindrical surface of the SWNT sidewall. Note that the operator Ω is not applicable to the coordinates of the atomic sites $\mathbf{R}_{hs}^u$ nor to the nearest-neighbor vectors $\mathbf{r}_s^\ell$ in the exponential factors of Eq. (8), because they are multiplied by the wave vectors $\mathbf{k}_i$ and $\mathbf{k}_f$ which are defined in the 2D reciprocal space of the unrolled graphene layer, according to the zone-folding scheme.[13] By selecting the right-handed Cartesian xyz-coordinate system, such that the graphene layer lies in the xy plane as shown in Fig. 1(a) and by aligning the rolled up SWNT along the z axis, we can write an explicit expression for the operator Ω in terms of the rotation operators Ω_α ($\alpha = x,y,z$) about the principal axes,

$$\Omega = \Omega_z(\Theta\varphi_{hs})\Omega_y\left(\frac{\pi}{6}-\theta\right)\Omega_x\left(\frac{\pi}{2}\right). \tag{10}$$

To align the cylinder along the z axis, the rotation operator $\Omega_x(\pi/2)$ in Eq. (10) is applied first. Then the graphene layer in the xz plane is rotated by the operator $\Omega_y(\pi/6-\theta)$ to account for the SWNT chirality. Finally, the graphene layer is rolled up into a cylinder of diameter d_t around the z axis by the operator $\Omega_z(\Theta\varphi_{hs})$, where φ_{hs} is the angular coordinate of the atomic site $\mathbf{R}_{hs}^u$ on the cylindrical surface of the nanotube, and Θ indicates the type of rolling done to the graphene layer, from the front to the back ($\Theta=+1$) or from the back to the front ($\Theta=-1$). Thus $\Theta=+1$ corresponds to AL (ZR) and $\Theta=-1$ to AR (ZL) handedness (see Sec. II). Using the rotation operators of Eq. (10), the angular coordinates of the atomic sites φ_{hs} and the angular shifts on the cylindrical surface between the nearest-neighbor carbon atoms φ_s^ℓ become

$$\varphi_{hs} = \frac{2}{d_t}\left[\Omega_y\left(\frac{\pi}{6}-\theta\right)\Omega_x\left(\frac{\pi}{2}\right)\mathbf{R}_{hs}^u\right]\cdot\hat{\mathbf{x}},$$

$$\varphi_s^\ell = \frac{2}{d_t}\left[\Omega_y\left(\frac{\pi}{6}-\theta\right)\Omega_x\left(\frac{\pi}{2}\right)\mathbf{r}_s^\ell\right]\cdot\hat{\mathbf{x}}. \tag{11}$$

By substituting the operator Ω of Eq. (10) into Eq. (8), we can write the dipole vector $\mathbf{D}$ in the form

$$\mathbf{D} = \frac{\sqrt{3}M_{\rm dip}}{aNU}\left[C_B^f{}^* C_A^i \sum_{u=1}^{U}\sum_{h=1}^{N} e^{i(\mathbf{k}_i-\mathbf{k}_f)\cdot\mathbf{R}_{hA}^u}\mathbf{d}_{hA} + C_A^f{}^* C_B^i \sum_{u=1}^{U}\sum_{h=1}^{N} e^{i(\mathbf{k}_i-\mathbf{k}_f)\cdot\mathbf{R}_{hB}^u}\mathbf{d}_{hB}\right], \tag{12}$$

where $\mathbf{d}_{hA}$ and $\mathbf{d}_{hB}$ are the atomic dipole vectors for electronic optical transitions from the A atom in the hth hexagon to its neighboring B atoms, and from the B atom in the hth hexagon to its neighboring A atoms, respectively. The atomic dipole vectors $\mathbf{d}_{hs}$ ($h=1,\ldots,N$ and $s=A,B$) are given by

$$\mathbf{d}_{hs} = \Omega_z(\Theta\varphi_{hs})\mathbf{d}_s,$$

$$\mathbf{d}_s = \sum_{\ell=1}^{3} e^{-i\mathbf{k}_f\cdot\mathbf{r}_s^\ell}\Omega_y\left(\frac{\pi}{6}-\theta\right)\Omega_x\left(\frac{\pi}{2}\right)\mathbf{r}_s^\ell, \tag{13}$$

where $\mathbf{d}_s$ ($s=A,B$) are the atomic dipole vectors in the unrolled graphene layer. Note that $\mathbf{d}_B = -\mathbf{d}_A^*$. The atomic dipole vectors $\mathbf{d}_s$ defined by Eq. (13) lie in the xz plane and therefore can be written in the form $\mathbf{d}_A = (d_x,0,d_z)$ and $\mathbf{d}_B = (-d_x^*,0,-d_z^*)$. In fact, this approach ignores the curvature of the SWNT sidewall. Because of the curvature, the three nearest-neighbor vectors $\Omega\mathbf{r}_s^\ell$ ($\ell=1,\ldots,3$) do not lie in the same plane when placed on the cylinder surface, giving rise to small components of the atomic dipole vectors $\mathbf{d}_{hs}$ in the direction normal to the SWNT sidewall. The corresponding small y components of the atomic dipole vectors $\mathbf{d}_s$ in the unrolled graphene layer are omitted for simplicity. However, including these components does not affect in any way the selection rules we are here concerned with. By applying the rotation operators $\Omega_z(\Theta\varphi_{hA})$ and $\Omega_z(\Theta\varphi_{hB})$ to the atomic dipole vectors $\mathbf{d}_A=(d_x,0,d_z)$ and $\mathbf{d}_B=(-d_x^*,0,-d_z^*)$ according to Eq. (13), we obtain

$$\mathbf{d}_{hA} = (\cos(\varphi_{hA})d_x, \Theta\sin(\varphi_{hA})d_x, d_z),$$

$$\mathbf{d}_{hB} = (-\cos(\varphi_{hB})d_x^*, -\Theta\sin(\varphi_{hB})d_x^*, -d_z^*). \tag{14}$$

The dipole vector $\mathbf{D}$ is thus given by Eqs. (12) and (14), where we only need to substitute the wave vectors $\mathbf{k}_J$ and the Cartesian and angular coordinates of the atomic sites $\mathbf{R}_{hs}^u$ and ϕ_{hs}, respectively.

The coordinates of the atomic sites in the unrolled graphene layer can be written in the form $\mathbf{R}_{hs}^u = u\mathbf{T}+\mathbf{R}_h+\mathbf{R}_s$ where $u\mathbf{T}$ points to the uth unit cell, $\mathbf{R}_h$ to the hth hexagon within the unit cell, and $\mathbf{R}_s$ to the sth carbon atom within the hexagon. The N hexagons in the unit cell are arranged equidistantly around the SWNT axis forming the angles of rotation $2\pi h/N$. The two hexagons separated by the smallest angle of rotation $2\pi/N$ are connected by the symmetry vector $\mathbf{R}=p\mathbf{a}_1+q\mathbf{a}_2$ in the unrolled graphene layer.[13] The symmetry vector applied N times forms a spiral of N hexagons which spans the circumference of the SWNT and covers $M=mp-nq$ unit cells,[13] $N\mathbf{R}=\mathbf{C}_h+M\mathbf{T}$. The SWNT unit cell consists of pieces of the M spirals located

within a cylindrical segment of length T. The coordinate of the hth hexagon in the SWNT unit cell is thus given by $\mathbf{R}_h = h\mathbf{R} - [hM/N]\mathbf{T}$ where $[\xi]$ indicates the integer part of ξ. Recalling that the graphene unit cells are in fact not hexagons but rather rhombi, we immediately obtain $\mathbf{R}_s = -\mathbf{r}_s^1/2$ [see Fig. 1(a)]. Finally, the coordinates of the atomic sites are given by $\mathbf{R}_{hs}^u = u\mathbf{T} + h\mathbf{R} - [hM/N]\mathbf{T} - \mathbf{r}_s^1/2$. Substituting $\mathbf{R}_{hs}^u$ into Eq. (11) yields the angular coordinates of the atomic sites $\varphi_{hs} = 2\pi h/N - \varphi_s^1/2$, where $\varphi_A^1 = -\varphi_B^1 = (2/\sqrt{3}) \times (a/d_t)\cos(\pi/6 - \theta)$ is the angular shift on the cylindrical surface between the A and B atoms of the graphene unit cell. The angular coordinates, thus obtained, define the atomic dipole vectors $\mathbf{d}_{hs}$ of Eq. (14). We now need to calculate the phase factors in the dipole vector $\mathbf{D}$ of Eq. (12).

The electronic wavevectors $\mathbf{k}_J$ $(J = \imath, f)$ from the phase factors of Eq. (12) are defined within the zone-folding scheme,[13] $\mathbf{k}_J = \mu_J \mathbf{K}_1 + k_J \mathbf{K}_2/|\mathbf{K}_2|$, where μ_J is the cutting line index, also referred to as the subband index, or the angular momentum in the circumferential direction of the SWNT, and k_J is the 1D wave vector in the axial direction of the SWNT. The wave vectors $\mathbf{K}_1$ and $\mathbf{K}_2$ define the separation between the adjacent cutting lines and the length of the cutting lines, respectively.[13] Within the $\mathbf{K}_1$-extended representation of the cutting lines,[17] μ_J varies in the range $1 - N/2 \leqslant \mu_J \leqslant N/2$ and k_J is in the range $-\pi/T < k_J \leqslant \pi/T$. For a SWNT of finite length L, the 1D wave vector k_J becomes quantized, so that $\mathbf{k}_J = \mu_J \mathbf{K}_1 + k_J \mathbf{K}_2/U$, where k_J is now an integer number varying in the range $1 - U/2 \leqslant k_J \leqslant U/2$. By defining the cutting line index change $\Delta\mu = \mu_f - \mu_\imath$ and the wave-vector change $\Delta k = k_f - k_\imath$, we can write the difference of the electronic wave vectors from the phase factors of Eq. (12) in the form $\mathbf{k}_\imath - \mathbf{k}_f = -\Delta\mu \mathbf{K}_1 - \Delta k \mathbf{K}_2/U$.

By substituting $\mathbf{k}_\imath - \mathbf{k}_f$ and $\mathbf{R}_{hs}^u$ into Eq. (12), the summation over the index u (over the SWNT unit cells) can be taken out of the squared brackets in the form $\Sigma_{u=1}^U \exp[-i(\Delta\mu \mathbf{K}_1 + \Delta k \mathbf{K}_2/U) \cdot u\mathbf{T}]$. The wave vectors $\mathbf{K}_1$ and $\mathbf{K}_2$ are defined as reciprocal-lattice unit vectors with respect to $\mathbf{C}_h$ and $\mathbf{T}$, that is, $\mathbf{K}_1 \cdot \mathbf{C}_h = \mathbf{K}_2 \cdot \mathbf{T} = 2\pi$ and $\mathbf{K}_1 \cdot \mathbf{T} = \mathbf{K}_2 \cdot \mathbf{C}_h = 0$.[13] The sum over the index u then becomes $\Sigma_{u=1}^U \exp[-i(2\pi u/U)\Delta k]$. The latter sum is equal to zero unless $\Delta k = 0$, and for such a case the sum is equal to U. We thus obtain the selection rule for the electronic wave vector along the SWNT axis, $\Delta k = 0$ or $k_f = k_\imath$, in agreement with the general property of momentum conservation. Summing Eq. (12) over the index h (over the graphene unit cells) leads to the selection rule for the cutting line index μ, as we will show in the next paragraph.

With the help of the selection rule $\Delta k = 0$ derived above, we can simplify the phase factors of Eq. (12) to the form $\exp[-i\Delta\mu \mathbf{K}_1 \cdot (h\mathbf{R} - \mathbf{r}_s^1/2)]$. Substituting the symmetry vector $N\mathbf{R} = \mathbf{C}_h + M\mathbf{T}$ and using the relations $\mathbf{K}_1 \cdot \mathbf{C}_h = 2\pi$ and $\mathbf{K}_1 \cdot \mathbf{T} = 0$, we obtain $\exp[-i\Delta\mu 2\pi h/N + i\Delta\mu \mathbf{K}_1 \cdot \mathbf{r}_s^1/2]$, where $\mathbf{K}_1 \cdot \mathbf{r}_s^1 = \varphi_s^1$ according to the definition of φ_s^1 in Eq. (11). By decomposing $\cos(\varphi_{hs})$ and $\sin(\varphi_{hs})$ of Eq. (14) into the sums and differences of complex exponents, the dipole vector $\mathbf{D}$ of Eq. (12) can be written as

$$D_x = \frac{1}{2}(C_{+1}S_{+1} + C_{-1}S_{-1}),$$

$$D_y = \Theta\frac{1}{2i}(C_{+1}S_{+1} - C_{-1}S_{-1}),$$

$$D_z = C_0 S_0, \tag{15}$$

where the following notation is used:

$$S_\ell = \frac{1}{N}\sum_{h=1}^{N} e^{-i(\Delta\mu - \ell)2\pi h/N},$$

$$C_0 = \frac{\sqrt{3}M_{\mathrm{dip}}}{a}[C_B^{f*} C_A^\imath d_z \xi_0 - C_A^{f*} C_B^\imath d_z^* \xi_0^*],$$

$$C_{\pm 1} = \frac{\sqrt{3}M_{\mathrm{dip}}}{a}[C_B^{f*} C_A^\imath d_x \xi_{\pm 1} - C_A^{f*} C_B^\imath d_x^* \xi_{\pm 1}^*],$$

$$\xi_\ell = e^{i(\Delta\mu - \ell)\varphi_A^1/2}. \tag{16}$$

The matrix element of Eq. (4) is proportional to the scalar product of the light polarization vector $\mathbf{P}_\rho$ $(\rho = a, e)$ and the dipole vector given by Eq. (15). One can see from Eq. (15) that the light polarized parallel to the SWNT axis $(\mathbf{P}_\rho = \hat{\mathbf{z}})$ selects the term S_0 in the matrix element, while the light polarized perpendicular to the SWNT axis $(\mathbf{P}_\rho = \hat{\mathbf{x}}$ or $\hat{\mathbf{y}})$ selects the terms S_{+1} and S_{-1}. The presence of the term S_ℓ $(\ell = 0, \pm 1)$ in the matrix element implies the optical selection rule $\Delta\mu = \ell$, or $\mu_f = \mu_\imath + \ell$, also written as $\mu \to \mu + \ell$, since $S_\ell = 1$ for $\Delta\mu = \ell$ and $S_\ell = 0$ otherwise, according to the definition of Eq. (16). We thus obtain the dipole selection rules for the optical electronic transitions, $\mu \to \mu$ for parallel polarization (z) and $\mu \to \mu \pm 1$ for perpendicular polarization (x or y).[1,2,4]

For circularly polarized light propagating along the SWNT axis (z), the light polarization vector is given by $\mathbf{P}_\rho = (1, \Upsilon\Lambda i, 0)$, where $\Lambda = +1$ for L and $\Lambda = -1$ for R helicity of light, indicating a rotation of the optical electric-field intensity $\mathbf{E}_\rho$ (where $\mathbf{E}_\rho \| \mathbf{P}_\rho$) to the L and to the R when looking along the light propagation direction (z), while $\Upsilon = +1$ for light absorption $(\rho = a)$ and $\Upsilon = -1$ for light emission $(\rho = e)$. Multiplying the dipole vector of Eq. (15) by the light polarization vector $\mathbf{P}_\rho = (1, \Upsilon\Lambda i, 0)$ with consequent substitution into the optical electronic transition matrix element given by Eq. (4) yields

$$M_{\mathrm{opt}}^\rho = i\frac{1}{2}\frac{e\hbar}{m\omega_\rho}\sqrt{\frac{I_\rho}{\epsilon c}} e^{i(\omega_f - \omega_\imath - \Upsilon\omega_\rho)t}[(1 + \Theta\Lambda\Upsilon)C_{+1}S_{+1} + (1 - \Theta\Lambda\Upsilon)C_{-1}S_{-1}]. \tag{17}$$

Either of the two terms in the squared brackets of Eq. (17) vanishes, depending on the sign of the product $\Theta\Lambda\Upsilon$. Remember that $\Theta = +1$ for AL (ZR) and $\Theta = -1$ for AR (ZL) handedness of SWNTs, $\Lambda = +1$ for L and $\Lambda = -1$ for R helicity of light, and $\Upsilon = +1$ (absorption, $\rho = a$) and $\Upsilon = -1$ (emission, $\rho = e$). The presence of the term S_ℓ in Eq. (17) indicates the selection rule $\Delta\mu = \ell$, or $\mu \to \mu + \ell$, as

TABLE I. The optical selection rules for circularly polarized light propagating along the axis of the chiral SWNT. The SWNT handedness is referred to as AL/ZR (armchair-left/zigzag-right, $\Theta=+1$) and AR/ZL (armchair-right/zigzag-left, $\Theta=-1$). The helicity of the light is referred to as L (left, $\Lambda=+1$) and R (right, $\Lambda=-1$). The two cases for light absorption ($\rho=a,\Upsilon=+1$) and light emission ($\rho=e,\Upsilon=-1$) are shown.

SWNT handedness	Light helicity L ($\Lambda=+1$)	Light helicity R ($\Lambda=-1$)
Light absorption ($\Upsilon=+1$)		
AL/ZR ($\Theta=+1$)	$\mu\rightarrow\mu+1$	$\mu\rightarrow\mu-1$
AR/ZL ($\Theta=-1$)	$\mu\rightarrow\mu-1$	$\mu\rightarrow\mu+1$
Light emission ($\Upsilon=-1$)		
AL/ZR ($\Theta=+1$)	$\mu\rightarrow\mu-1$	$\mu\rightarrow\mu+1$
AR/ZL ($\Theta=-1$)	$\mu\rightarrow\mu+1$	$\mu\rightarrow\mu-1$

discussed above. The selection rules obtained from Eq. (17) for different SWNT handedness, for different light helicity, and for light absorption and emission processes are summarized in Table I. In zigzag and armchair achiral SWNTs, circularly polarized light induces both electronic transitions $\mu\rightarrow\mu+1$ and $\mu\rightarrow\mu-1$ simultaneously, since both the AL ($\Theta=+1$) and AR ($\Theta=-1$) chiral forms correspond to the same atomic structure of achiral SWNTs. In contrast, only one of the two electronic transitions, either $\mu\rightarrow\mu+1$ or $\mu\rightarrow\mu-1$, is allowed in chiral SWNTs, depending on whether the light is absorbed or emitted, on the helicity of the light, and on the handedness of the SWNT.

The matrix element given by Eq. (17) describes the transition between electronic states $(\mu_\imath,k_\imath)$ and (μ_f,k_f), where $\mu_f=\mu_\imath-1$ or $\mu_\imath+1$, according to the selection rules listed in Table I, and $k_f=k_\imath$. The total electronic optical transition rate is given by

$$W^{\rho}_{\rm opt}=\frac{1}{\tau_\rho}\sum_{\mu_\imath k_\imath}\left|-\frac{i}{\hbar}\int_0^{\tau_\rho}dtM^{\rho}_{\rm opt}\right|^2 \tag{18}$$

within first-order time-dependent perturbation theory, where the summation over the final states (μ_f,k_f) is omitted because of the aforementioned selection rules, and τ_ρ is the electron-photon interaction time related to the frequency broadening of light $\Delta\omega_\rho$ by the uncertainty principle, $\tau_\rho=2\pi/\Delta\omega_\rho$. The value of $\Delta\omega_\rho=10\ {\rm cm}^{-1}$ typical for the laser beam corresponds to $\tau_\rho=0.5$ ps. Integrating the time dependence of the matrix element in Eq. (18) yields

$$W^{\rho}_{\rm opt}=\sum_{\mu_\imath k_\imath}\frac{2\pi}{\hbar}|M^{\rho}_{\rm opt}|^2\left[\frac{4\sin^2[(\omega_f-\omega_\imath-\Upsilon\omega_\rho)\tau_\rho/2]}{2\pi\hbar(\omega_f-\omega_\imath-\Upsilon\omega_\rho)^2\tau_\rho}\right]. \tag{19}$$

In the weak interaction limit, $\tau_\rho\rightarrow\infty$ and the expression in the square brackets of Eq. (19) becomes a delta function, $\delta(E_f-E_\imath-\Upsilon\hbar\omega_\rho)$, reflecting energy conservation. Summing the expression in the squared brackets over the states $(\mu_\imath,k_\imath)$ in Eq. (19) gives the joint density of electronic states at the resonant transition energy, $E_f-E_\imath=\Upsilon\hbar\omega_\rho$, and Eq. (19) then becomes Fermi's golden rule.

IV. DISCUSSION

The dipole selection rules for SWNTs predict optical electronic transitions $\mu\rightarrow\mu$ and $\mu\rightarrow\mu\pm1$ for light polarized parallel and perpendicular to the SWNT axis, respectively.[1,2,4] For perpendicular polarization, the optical field gains a phase factor when the cylindrical SWNT surface is unrolled into the flat graphene layer,[1,17] yielding a change of electronic momentum in the unfolded 2D Brillouin zone, $\Delta\mathbf{k}=\pm\mathbf{K}_1$, which is equivalent to a transition to the adjacent cutting line, $\mu\rightarrow\mu\pm1$. The selection rule $\mu\rightarrow\mu\pm1$ becomes more specific in the case of circularly polarized light propagating along the axis of a chiral SWNT, either $\mu\rightarrow\mu+1$ or $\mu\rightarrow\mu-1$, depending on whether the light is absorbed or emitted, on the helicity of the light, as shown in Ref. 10, and on the handedness of the SWNT. All these cases are summarized in Table I.

The same selection rules derived in Sec. III from perturbation theory can be obtained directly from group theory using the symmetry properties of chiral SWNTs. The total symmetry of a chiral SWNT is expressed by the group C_N, where N is the number of hexagons in the SWNT unit cell.[13] The electric dipole Hamiltonian given by Eq. (2) transforms as one of the two partners of the two-dimensional representation E_1, depending on the light absorption or emission process, on the light helicity, and on the SWNT handedness. Calculating direct products of E_1 with other irreducible representations of group C_N yields the selection rules listed in Table I. The selection rules are therefore independent of the tight-binding representation of the Bloch functions in Eq. (7) and they are primarily determined by the symmetry properties of chiral SWNTs. The presence of a screw axis in chiral SWNTs thus provides a possibility for the optical determination of the SWNT handedness.

The symmetry properties of chiral SWNTs are inherited from the symmetry properties of the graphene layer. The presence of the two inequivalent atomic sites (A and B, as shown in Fig. 1(a)) in the unit cell of the graphene layer, related to each other by the 2D spatial inversion in the graphene plane (the center of inversion is the center of a hexagon in the graphene layer), results in two inequivalent degeneracy points (hexagonal corners K and K') in the first Brillouin zone of the graphene layer related to each other by time-reversal symmetry.[13] The time-reversal symmetry and the spatial inversion symmetry impose the following constraints on the electronic dispersion relations in the graphene layer, $E_{J\bar{s}}(-\mathbf{k})=E_{Js}(\mathbf{k})$ and $E_{Js}(-\mathbf{k})=E_{Js}(\mathbf{k})$, respectively, where $J=v,c$ is the band index, $s=\uparrow\downarrow$ is the spin of the electron (where $\bar{s}$ is directed opposite to s), and $\mathbf{k}$ is the 2D wave vector.

When the 2D graphene layer is rolled up into the 1D SWNT, the 2D electronic dispersion relations of the graphene layer are folded into the 1D electronic dispersion relations of the SWNT,[13] namely, the 2D wave vector $\mathbf{k}$ splits into the 1D wave vector k and the cutting line index μ (also referred to as the subband index or the angular momentum). The time-reversal symmetry and the 1D spatial inversion along the SWNT axis now yield $E_{J\bar{s}}(-\mu,-k)=E_{Js}(\mu,k)$ and $E_{Js}(\mu,-k)=E_{Js}(\mu,k)$, respectively, for zigzag and

armchair achiral SWNTs. For chiral SWNTs, the spatial inversion symmetry is broken, as it inverts the SWNT handedness. Correspondingly, the electronic dispersion relations in chiral SWNTs are only constrained by time-reversal symmetry, which yields $E_{J\bar{s}}(-\mu,-k)=E_{Js}(\mu,k)$. Thus, the electronic dispersion relations in chiral SWNTs are asymmetric in k with respect to the center of the 1D Brillouin zone ($k=0$), and this asymmetry is responsible for the optical activity of chiral SWNTs.[10,18]

In fact, however, time-reversal symmetry prevents observation of optical activity in chiral SWNTs. Time-reversal symmetry requires that the interband electronic transition $\mu \rightarrow \mu+1$ (near the K point in the unfolded 2D Brillouin zone) for a given spin state s has the same transition energy as the $-\mu \rightarrow -\mu-1$ (near the K' point in the unfolded 2D Brillouin zone) for the opposite spin state $\bar{s}$, and vice versa. This implies that the two different interband electronic transitions $\mu \rightarrow \mu+1$ and $\mu \rightarrow \mu-1$ yield the same optical response, when time-reversal symmetry is preserved. That is, no optical activity would be expected and the SWNT handedness would not be distinguished by optical spectroscopy, according to the selection rules in Table I, unless time-reversal symmetry is broken. Once time-reversal symmetry is broken, the spin-orbit interaction must be taken into account. The latter, however, is known to be weak in carbon materials, and is hereby incorporated by using the $\mathbf{k}\cdot\mathbf{p}$ perturbation method in graphite[19] and in SWNTs.[20] Besides, inclusion of spin-orbit coupling yields only small corrections to the optical activity effects.[21] The optical activity effects in chiral SWNTs are thus primarily determined by breaking the time-reversal symmetry.

Once the time-reversal symmetry is broken, the presence of a screw axis in chiral SWNTs gives rise to their optical activity through appearance of the odd-in-k terms in the electronic dispersion relations.[10,18] Optical activity consists of the circular dichroism (difference in absorption of L and R circularly polarized light) and the circular birefringence (the rotation of light polarization plane), the two conjugate effects being typical of chiral organic molecules and enantiomorphic crystals (natural optical activity),[22] as well as of homomorphic crystals under uniaxial stress (stress-induced optical activity)[21] and in the presence of an axial magnetic field (magnetically induced optical activity).[22] No optical activity, however, is expected in SWNT bundles, since both AL and AR handed SWNTs are equally present within the bundle, assuming chiral homogeneity of the synthesis process. Once the separation of chiral SWNTs according to their handedness succeeds, the efficiency of such a separation can be monitored by optical techniques, utilizing the effects of natural circular dichroism and natural circular birefringence. One of the possible separation mechanisms can be related to the recently reported liquid ion exchange chromatography of DNA wrapped SWNTs,[23] because of the intrinsic handedness of the single-stranded DNA molecules.

The time-reversal symmetry is broken by the spatial inhomogeneity of the optical field along the length of the SWNT. Phenomenologically, the spatial inhomogeneity of the optical field is described[24] by the third-rank tensor term γ_{ijl} in the dielectric function ϵ_{ij}, given the electric displacement flux density $D_i=\epsilon_{ij}E_j+\gamma_{ijl}(dE_j/dr_l)$ for the optical electric-field intensity E_j. In other words, the term γ_{ijl} reflects the dependence of the dielectric function ϵ_{ij} on the photon wave vector κ_l, $\gamma_{ijl}=-\Upsilon i(d\epsilon_{ij}/d\kappa_l)$, as follows from the vector potential of Eq. (3). The term γ_{ijl} is calculated in Ref. 9 for chiral SWNTs giving rise to their natural optical activity. The natural optical activity is thus induced by the spatial inhomogeneity of the optical field propagating in media which lack spatial inversion symmetry.

The spatial inhomogeneity of the optical field is expressed by the photon wave vector $\boldsymbol{\kappa}_\rho$ ($\rho=a,e$) in Eq. (3). For light propagating perpendicular to the SWNT axis, $\boldsymbol{\kappa}_\rho$ can be neglected, since the SWNT diameter d_t is much smaller than the wavelength of light λ_ρ, $d_t \ll \lambda_\rho$. In contrast, the SWNT length L is of the order of λ_ρ, $L \sim \lambda_\rho$, so that the optical field is sufficiently inhomogeneous for light propagating along the SWNT axis. Taking into account the photon wave vector $\boldsymbol{\kappa}_\rho$ in Eq. (8) results in the dipole vector

$$\begin{aligned}\mathbf{D}&=\langle\Psi_f|e^{\Upsilon i\boldsymbol{\kappa}_\rho\cdot\mathbf{r}}\boldsymbol{\nabla}|\Psi_\iota\rangle\\&=\frac{\sqrt{3}}{UNa}\Bigg[C_B^{f}{}^{*}C_A^{\iota}\sum_{u=1}^{U}\sum_{h=1}^{N}e^{i(\mathbf{k}_\iota-\mathbf{k}_f+\Upsilon\boldsymbol{\kappa}_\rho)\cdot\mathbf{R}_{hA}^{u}}\\&\quad\times\sum_{\ell=1}^{3}M_A^{\ell\rho}e^{-i[\mathbf{k}_f-\Upsilon(1/2)\boldsymbol{\kappa}_\rho]\cdot\mathbf{r}_A^{\ell}}\Omega\mathbf{r}_A^{\ell}\\&\quad+C_A^{f}{}^{*}C_B^{\iota}\sum_{u=1}^{U}\sum_{h=1}^{N}e^{i(\mathbf{k}_\iota-\mathbf{k}_f+\Upsilon\boldsymbol{\kappa}_\rho)\cdot\mathbf{R}_{hB}^{u}}\\&\quad\times\sum_{\ell=1}^{3}M_B^{\ell\rho}e^{-i[\mathbf{k}_f-\Upsilon(1/2)\boldsymbol{\kappa}_\rho]\cdot\mathbf{r}_B^{\ell}}\Omega\mathbf{r}_B^{\ell}\Bigg].\end{aligned}\tag{20}$$

Note that the photon wave vector $\boldsymbol{\kappa}_\rho$ changes the electronic optical transition matrix elements between the nearest-neighbor carbon atoms, so that Eq. (9) becomes

$$\langle\phi(\mathbf{r}-\tfrac{1}{2}\mathbf{r}_s^{\ell})|e^{\Upsilon i\boldsymbol{\kappa}_\rho\cdot\mathbf{r}}\boldsymbol{\nabla}|\phi(\mathbf{r}+\tfrac{1}{2}\mathbf{r}_s^{\ell})\rangle=\frac{\sqrt{3}M_s^{\ell\rho}\mathbf{r}_s^{\ell}}{a}.\tag{21}$$

Because the lattice constant of the graphene layer $a=0.246$ nm is negligible compared to the wavelength of light λ_ρ, the matrix elements $M_s^{\ell\rho}$ of Eq. (21) can be considered equal to the matrix element M_{dip} of Eq. (9), $M_s^{\ell\rho}=M_{\mathrm{dip}}$. Thus, the only difference between the dipole vectors of Eqs. (8) and (20) is the wave-vector change from $(\mathbf{k}_\iota-\mathbf{k}_f)$ to $(\mathbf{k}_\iota-\mathbf{k}_f+\Upsilon\boldsymbol{\kappa}_\rho)$ and from $\mathbf{k}_f$ to $(\mathbf{k}_f-\Upsilon\frac{1}{2}\boldsymbol{\kappa}_\rho)$ in the phase factors. This change reflects conservation of the electronic momentum along the SWNT axis, $\Delta k=k_f-k_\iota=\Upsilon\kappa_\rho=\Upsilon 2\pi/\lambda_\rho$, and does not affect the selection rules for the cutting line indices μ_f and μ_ι summarized in Table I.

We now consider the effect of the photon wave vector ($\boldsymbol{\kappa}_\rho$) on the optical absorption spectra ($\rho=a$) of chiral SWNTs. We select the (20,10) semiconducting SWNT of diameter $d_t=2.07$ nm and chiral angle $\theta=19.1°$ for demonstration purpose. The electronic band structure for a (20,10) SWNT of AL handedness is shown in Figs. 2(a) and 2(b), which depict, respectively, those electronic subbands which

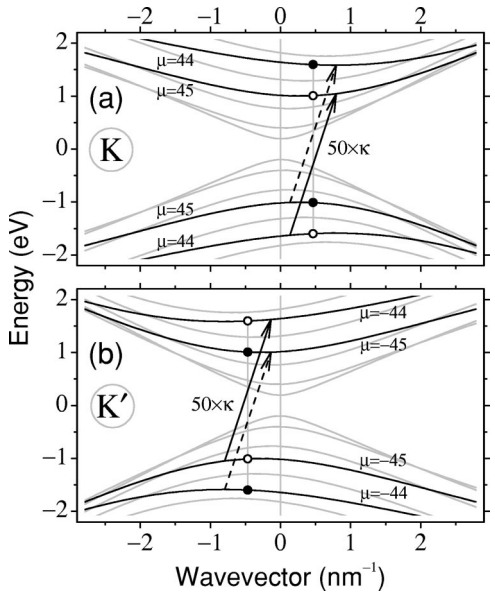

FIG. 2. Electronic band structure of an AL handed (20,10) SWNT in the zone-folding scheme (Ref. 13) using the nearest-neighbor tight-binding approximation and transfer integral $t = 2.89$ eV (Ref. 25). Only subbands in the vicinity of the (a) K and (b) K' points of the unfolded 2D Brillouin zone are shown, for which the cutting line indices are $\mu > 0$ and $\mu < 0$, respectively. The electronic subbands are indexed by $|\mu| = 47,46,48,45,49,44,50$ and are ordered according to increasing energy separation from the Fermi level $E_F = 0$. Subbands $|\mu| = 45,44$ are shown as black curves and labels, while the other subbands are shown as gray curves. Open and solid dots show vertical transitions $\mu \rightarrow \mu + 1$ ($\mu = 44, -45$) and $\mu \rightarrow \mu - 1$ ($\mu = 45, -44$), associated with the $E_{\mu,\mu\pm1} = 2.60$ eV VHS in the JDOS. Solid and dashed arrows show actual electronic transitions involving the momentum change by the photon wave vector (κ), which is increased by 50 times for demonstration purpose (50κ).

are mapped to the vicinity of the K and K' points of the unfolded 2D Brillouin zone (see figure caption for details). The vertical gray lines connecting the open and solid dots show $\mu \rightarrow \mu \pm 1$ electronic transitions for the $|\mu| = 44$ and 45 subbands, giving rise to an $E_{\mu,\mu\pm1} = 2.60$ eV van Hove singularity (VHS) in the joint density of states (JDOS). The open and solid dots indicate $\mu \rightarrow \mu + 1$ and $\mu \rightarrow \mu - 1$ electronic transitions, respectively. The transition energy $E_{\mu,\mu\pm1} = 2.60$ eV is the same for both processes $\mu \rightarrow \mu + 1$ and $\mu \rightarrow \mu - 1$ as long as we neglect the photon wave vector κ_ρ ($\rho = a, e$), i.e., while we assume the electronic transitions being vertical. In fact, however, the photon wave vector κ_ρ changes the electronic wave vector, $k_f - k_i = \Upsilon \kappa_\rho$, for light propagating along the SWNT axis. The solid and dashed arrows in Fig. 2 show the real nonvertical electronic transitions $\mu \rightarrow \mu + 1$ and $\mu \rightarrow \mu - 1$, respectively, for the absorption ($\rho = a$) of L and R circularly polarized photon propagating in the positive direction of the z axis ($\kappa_\rho > 0$). For the photon wavelength 476 nm (2.60 eV), the photon wave vector $\kappa_\rho = 1.32 \times 10^{-2}$ nm^{-1} is about 200 times smaller than the maximum electronic wave vector $k_j = \pi/T = 2.79$ nm^{-1} at the edge of the 1D Brillouin zone, where $T = 1.13$ nm is the length of the unit cell for the (20,10) SWNT. Correspondingly, the photon wave vector κ_ρ in the band diagram of Fig. 2 is increased by 50 times in order to observe its effect on the electronic transitions $\mu \rightarrow \mu \pm 1$.

The solid and dashed arrows in Fig. 2 connect the electronic states in the valence and conduction subbands at which these subbands have the same slope, i.e., where the VHSs appear in the JDOS. These VHSs depicted by the solid and dashed arrows in Fig. 2 differ from the VHS $E_{\mu,\mu\pm1} = 2.60$ eV which involves vertical electronic transitions neglecting the photon wave vector κ_ρ, as shown by the open and solid dots in Fig. 2. Let us consider the $\mu \rightarrow \mu + 1$ transition in the vicinity of the K point, where $\mu_i = 44$ and $\mu_f = 45$, as shown in Fig. 2(a). The electronic states in the valence and conduction bands for the VHS in the JDOS are shifted by the photon wave vector κ_ρ from the open dots, as indicated by the solid arrow. Because the energy extrema in the valence and conduction bands appear, respectively, at wave vectors above and below the VHS wave vectors (the open dots), the photon wave vector κ_ρ (the solid arrow) shifts the VHS wave vectors (the open dots) further away from the energy extrema in the valence and conduction bands. The photon wave vector κ_ρ thus gives an increase to the energy of the VHS in the JDOS for the $\mu \rightarrow \mu + 1$ transition. The same increase takes place for the $\mu \rightarrow \mu + 1$ transition in the vicinity of the K' point, where transitions between $\mu_i = -45$ and $\mu_f = -44$ contribute, as shown in Fig. 2(b) by the solid arrow. In contrast, the photon wave vector κ_ρ gives a decrease to the energy of the VHS in the JDOS for $\mu \rightarrow \mu - 1$ transitions (the dashed arrows in Fig. 2). The energy of the VHS in the JDOS for the vertical electronic transitions, $E_{\mu,\mu\pm1} = 2.60$ eV, thus splits into two different energies, slightly above and slightly below the value of 2.60 eV, for the $\mu \rightarrow \mu + 1$ and $\mu \rightarrow \mu - 1$ transitions, respectively. We thus expect to observe slightly different optical absorption spectra for the light of L and R helicity (circular dichroism) as well as for the SWNTs of L and R handedness, because only one of two transitions $\mu \rightarrow \mu \pm 1$ is allowed in these cases according to the optical selection rules summarized in Table I.

We calculated the electronic optical transition rates of Eq. (19) for light absorption ($\rho = a$) as a function of the light wavelength, i.e., the optical absorption spectra, for the (20,10) SWNTs of AL and AR handedness, and for L and R helicity of the light, using light broadening $\Delta\omega_a = 10$ cm^{-1} and the electronic band structure shown in Fig. 2 (in the present discussion, we consider the real photon wave vector value, not increased by 50 times as in Fig. 2). The optical absorption spectra are shown in Fig. 3(a), where the labels AL and AR indicate the SWNT handedness, while PL and PR denote the photon helicity. The solid and dashed curves in Fig. 3(a) correspond to the cases of matched and mismatched SWNT handedness and light helicity, respectively. For comparison, Fig. 3(b) shows the JDOS profile of a (20,10) SWNT for vertical $\mu \rightarrow \mu \pm 1$ electronic transitions (neglecting the photon wave vector κ_a), where the electronic transition energy is measured in nanometers for direct comparison with the optical absorption spectra in Fig. 3(a). The spike in the JDOS profile around 476 nm is due to the

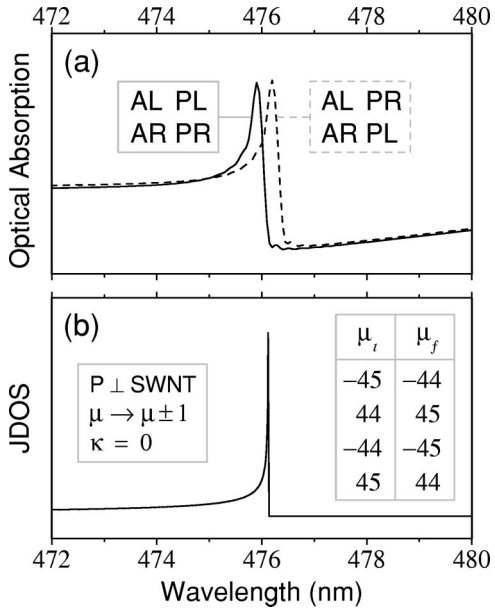

FIG. 3. (a) Optical absorption spectra for (20,10) SWNTs of AL and AR handedness and for L and R circularly polarized photons labeled by PL and PR, respectively, taking into account the photon wave vector (κ). (b) JDOS for $\mu \rightarrow \mu \pm 1$ vertical electronic transitions in AL and AR (20,10) SWNTs, neglecting the photon wave vector (κ). Calculations are based on Eq. (19) with light broadening $\Delta\omega = 10\ \mathrm{cm}^{-1}$ and the electronic band structure of Fig. 2. A VHS at 476 nm (2.60 eV) arises from transitions between subbands $|\mu| = 45,44$.

$E_{\mu,\mu\pm1} = 2.60$ eV VHS arising from four different electronic transitions between the subbands $|\mu| = 44$ and 45 [see tabular inset in Fig. 3(b), and the open and solid dots in Fig. 2 connected by the vertical gray lines]. By comparing Figs. 3(a) and 3(b), one can see that the optical absorption spectra pretty much follow the JDOS profile, being up-shifted or down-shifted in energy, depending on the SWNT handedness and on the light helicity, because of the photon wave vector κ_a, as discussed above. When the SWNT handedness and the light helicity match [see the solid curve in Fig. 3(a) and the solid arrows in Fig. 2], the VHS energy is downshifted in wavelength (up-shifted in energy), while for mismatched SWNT handedness and light helicity [the dashed curve in Fig. 3(a) and the dashed arrows in Fig. 2], the VHS energy is up-shifted in wavelength (down-shifted in energy), in agreement with our predictions given above for the discussion of the electronic transitions in Fig. 2. The splitting in wavelength between the solid and dashed curves in Fig. 3(a) is about 0.3 nm, which gives 0.06% when divided by the wavelength 476 nm. The small magnitude of the splitting (0.06%) is related to the small magnitude of the photon wave vector κ_a compared to the electronic wave vectors k_i and k_f (0.5 %), and also is related to the relatively flat valence and conduction bands in the vicinity of electronic states where the VHS in the JDOS occurs. We can expect a larger magnitude of the splitting in the low-quantum-number limit (the long-wavelength limit) where the electronic bands are less flat. Thus, it should be possible to observe the natural circular dichroism and the natural circular birefringence experimentally, though the experimental condition for observation is challenging. Such observation will be general for understanding many chiral nanomaterials.

The electronic transitions $\pm|\mu| \rightarrow \pm|\mu| \pm 1$ [the solid arrow in Fig. 2(a) and the dashed arrow in Fig. 2(b)] and $\pm|\mu| \rightarrow \pm|\mu| \mp 1$ (the other two arrows in Fig. 2) give rise to a single VHS in the JDOS profile of Fig. 3(b) because of the symmetry between the valence and conduction bands in Fig. 2. The electronic band structure shown in Fig. 2 is calculated in the nearest-neighbor tight-binding approximation with only one parameter, the transfer integral $t = 2.89$ eV, fitted to RRS data for $\mu \rightarrow \mu$ transitions in SWNTs.[25] While the asymmetry between the valence and conduction bands is not detected in optical studies for $\mu \rightarrow \mu$ transitions, it gives rise to a splitting in energy between the two VHSs in the JDOS for $\pm|\mu| \rightarrow \pm|\mu| \pm 1$ and $\pm|\mu| \rightarrow \pm|\mu| \mp 1$ transitions. Namely, the VHS $E_{\mu,\mu\pm1} = 2.60$ eV for the (20,10) SWNT shown in Fig. 3(b) splits in energy into $E_{\pm|\mu|,\pm|\mu|\pm1} = 2.82$ eV and $E_{\pm|\mu|,\pm|\mu|\mp1} = 2.67$ eV when using transfer integral $t = 3.033$ eV and overlap integral $s = 0.129$ fitted to the electronic band structure of graphite calculated from an *ab initio* variational approach,[13] the latter parameter being responsible for the asymmetry between the valence and conduction bands in graphite. The VHS splitting in energy yields the optical absorption peak splitting in wavelength. The two optical absorption peaks appear in Fig. 3(a) at 440 nm and 464 nm wavelength. The optical absorption peaks are thus split by 5% and by probing the splitting we can measure experimentally the asymmetry between the valence and conduction bands.

The asymmetry between the valence and conduction bands, if any, splits the VHS in the JDOS for the perpendicular polarization, but does not affect the optical activity of chiral SWNTs. Both components of the split VHS in the optical absorption spectra simultaneously up-shift or down-shift in energy when changing the light helicity or the SWNT handedness, i.e., for $\mu \rightarrow \mu + 1$ or $\mu \rightarrow \mu - 1$ transitions, respectively. Using the tight-binding parameters for graphite,[13] the two optical absorption peaks at 440 nm (transitions $44 \rightarrow 45$ and $-44 \rightarrow -45$ in Fig. 2) and 464 nm (transitions $45 \rightarrow 44$ and $-45 \rightarrow -44$ in Fig. 2) are shifted simultaneously in wavelength by 0.3 nm for opposite light helicity or SWNT handedness. Using various electronic band-structure models may significantly change the wavelengths of the optical absorption peaks (440 nm and 464 nm) and the spacing between them (24 nm), but the change in the optical activity shift (0.3 nm) is expected to be only minor, as long as the band-structure model reflects the symmetry of the π and π^* electronic states, because the latter shift is induced by the photon wave vector $\boldsymbol{\kappa}_\rho$ independent of the band-structure model. However, if the electronic states of different symmetry (σ and π^*) are involved in the optical transitions at the same wavelength, as happens for SWNTs in a certain diameter range according to linear augmented plane-wave calculations,[26] the effect of the SWNT handedness and light helicity on the optical absorption spectra must be reconsidered, as the selection rules change.

Apart from the σ-π^* electronic transitions, the σ states are known to mix with the π states in smaller diameter

SWNTs due to the curvature of the SWNT sidewall. The sidewall curvature does not affect the dipole selection rules for the π-π^* electronic transitions, as discussed previously in Sec. III. As for the σ-π hybridization in smaller d_t SWNTs, the tight-binding approximation is shown to describe the electronic transition energies of SWNTs for $d_t > 1.1$ nm with a precision of 10 meV in the wavelength range of visible light (488–785 nm).[27] The electronic transition energies in SWNTs of smaller diameters tend to downshift from the predictions of the tight-binding approximation by 20 meV for $d_t = 0.8$ nm,[27] yet the optical activity wavelength shift (0.3 nm) is hardly affected by the σ-π hybridization. The optical activity wavelength shift is only related to the curvature of the electronic band, being induced by the photon wave vector $\boldsymbol{\kappa}_\rho$ which breaks time-reversal symmetry.

The time-reversal symmetry can also be broken by a magnetic field applied parallel to the SWNT axis,[18] giving rise to an asymmetry in the electronic dispersion relations, which in turn yields a magnetically induced optical activity of chiral SWNTs, though the measurement of these effects requires a high magnetic field. The magnetically induced optical activity, also known as the Faraday effect, is phenomenologically described[24] by the third-rank tensor term γ_{ijl} in the dielectric function ϵ_{ij}, where the electric displacement flux density $D_i = \epsilon_{ij}E_j + \gamma_{ijl}E_jH_l$ depends on the external magnetic-field intensity H_l.

The magnetic-flux density $B\hat{\mathbf{z}}$ changes the phase factors of the electronic wave functions, shifting the electronic wave vectors in the circumferential direction of the SWNT (along the $\mathbf{K}_1$ wave vector in the unfolded 2D Brillouin zone of the graphene layer) by $\phi/(\pi d_t \phi_0)$, where ϕ is the magnetic flux penetrating the cross section of the SWNT, $\phi = B\pi d_t^2/4$, and $\phi_0 = h/e = 4135.6\ \mathrm{T\,nm^2}$ is the flux quantum.[13] The wave-vector shift splits the $\pm|\mu| \rightarrow \pm|\mu| \pm 1$ transitions in energy, up-shifting the energy of the $|\mu| \rightarrow |\mu| + 1$ transition and down-shifting the energy of the $-|\mu| \rightarrow -|\mu| - 1$ transition in the case of $B > 0$, yielding a splitting in energy of the VHS in the JDOS. The VHS splitting can be estimated by using the linear electronic dispersion approximation around the K and K' points in the unfolded 2D Brillouin zone,[13] $E_{v,c} = \mp(\sqrt{3}/2)tka$. The VHS splitting is given by $\Delta E = (\sqrt{3}/2)taBd_t/\phi_0$. Using the parameters $t = 2.89$ eV, $a = 0.246$ nm, and $d_t = 2.07$ nm, we obtain the VHS splitting of $\Delta E = 1.5$ meV for the large magnetic-flux density $B = 5$ T. The VHS splitting yields an optical absorption peak splitting of 0.3 nm or 0.06% for opposite light helicity or SWNT handedness. The magnetically induced optical activity for a magnetic-flux density $B = 5$ T is thus comparable to the natural optical activity in chiral SWNTs.

V. SUMMARY

The interband electronic optical transitions in chiral SWNTs with circularly polarized light propagating along the axis of the SWNTs are governed by different selection rules depending on the SWNT handedness and on the light helicity. The difference in the selection rules related to the presence of a screw axis in chiral SWNTs gives rise to their optical activity, when the time-reversal symmetry is broken. The time-reversal symmetry is broken by the spatial inhomogeneity of the optical field, yielding a natural circular dichroism and a natural circular birefringence (the natural optical activity) found in other chiral systems. The time-reversal symmetry can also be broken by an axial magnetic field yielding magnetically induced circular dichroism and magnetically induced circular birefringence (magnetically induced optical activity). The interband electronic optical transition matrix elements calculated for chiral SWNTs placed in an inhomogeneous optical field and in an axial magnetic field indicate their optical activity within a single-electron approximation. Phenomenologically, the optical activity of chiral SWNTs is related to the third-rank tensor term in the dielectric function. The optical activity of chiral SWNTs can be used for the optical determination of the SWNT handedness.

ACKNOWLEDGMENTS

The authors thank Professor M. A. Pimenta for valuable discussions. The MIT authors acknowledge support under NSF Grant No. DMR 01-16042. R. S. and A. G. acknowledge a Grant-in-Aid (Grant No. 13440091) from the Ministry of Education, Japan. A. J. and A. G. S. F. acknowledge financial support from CNPq-Brazil (Profix) and CAPES-Brazil (Prodoc).

[1] H. Ajiki and T. Ando, Physica B **201**, 349 (1994).
[2] I. Božović, N. Božović, and M. Damnjanović, Phys. Rev. B **62**, 6971 (2000).
[3] G.S. Duesberg, I. Loa, M. Burghard, K. Syassen, and S. Roth, Phys. Rev. Lett. **85**, 5436 (2000).
[4] A. Grüneis, R. Saito, Ge.G. Samsonidze, T. Kimura, M.A. Pimenta, A. Jorio, A.G. Souza Filho, G. Dresselhaus, and M.S. Dresselhaus, Phys. Rev. B **67**, 165402 (2003).
[5] A. Jorio, M.A. Pimenta, A.G. Souza Filho, Ge.G. Samsonidze, A.K. Swan, M.S. Ünlü, B.B. Goldberg, R. Saito, G. Dresselhaus, and M.S. Dresselhaus, Phys. Rev. Lett. **90**, 107403 (2003).
[6] H.H. Gommans, J.W. Alldredge, H. Tashiro, J. Park, J. Magnuson, and A.G. Rinzler, J. Appl. Phys. **88**, 2509 (2000).
[7] Y. Zhang, A. Chang, J. Cao, Q. Wang, W. Kim, Y. Li, N. Morris, E. Yenilmez, J. Kong, and H. Dai, Appl. Phys. Lett. **79**, 3155 (2001).
[8] J.B. Peatross, *Physics of Light and Optics* (Brigham Young University, 2001), see http://optics.byu.edu/BYUOpticsTextbook.htm.
[9] S. Tasaki, K. Maekawa, and T. Yamabe, Phys. Rev. B **57**, 9301 (1998).
[10] E.L. Ivchenko and B. Spivak, Phys. Rev. B **66**, 155404 (2002).
[11] J.W.G. Wildöer, L.C. Venema, A.G. Rinzler, R.E. Smalley, and C. Dekker, Nature (London) **391**, 59 (1998).

[12] R.R. Meyer, S. Friedrichs, A.I. Kirkland, J. Sloan, J.L. Hutchison, and M.L.H. Green, J. Microsc. **212**, 152 (2003).
[13] R. Saito, G. Dresselhaus, and M.S. Dresselhaus, *Physical Properties of Carbon Nanotubes* (Imperial College Press, London, 1998).
[14] Here we follow the definition of the chiral angle θ taken from Ref. 13 where θ increases in a clockwise direction, as shown in Fig. 1(a).
[15] R. Saito, A. Grüneis, Ge.G. Samsonidze, G. Dresselhaus, M.S. Dresselhaus, A. Jorio, L.G. Cançado, M.A. Pimenta, and A.G. Souza Filho, Appl. Phys. A: Mater. Sci. Process **78**, 1099 (2004).
[16] J. Jiang, R. Saito, A. Grüneis, G. Dresselhaus, and M.S. Dresselhaus (unpublished).
[17] Ge.G. Samsonidze, R. Saito, A. Jorio, M.A. Pimenta, A.G. Souza Filho, A. Grüneis, G. Dresselhaus, and M.S. Dresselhaus, J. Nanosci. Nanotechnol. **3**, 431 (2003).
[18] O.V. Kibis, Physica E (Amsterdam) **12**, 741 (2002).
[19] G. Dresselhaus and M.S. Dresselhaus, Phys. Rev. **140**, A401 (1965).
[20] T. Ando, J. Phys. Soc. Jpn. **69**, 1757 (2000).
[21] B. Koopmans, P.V. Santos, and M. Cardona, Phys. Status Solidi B **205**, 419 (1998).
[22] L.D. Barron, Nature (London) **405**, 895 (2000).
[23] M. Zheng, A. Jagota, E.D. Semke, B.A. Diner, R.S. McLean, S.R. Lustig, R.E. Richardson, and N.G. Tassi, Nat. Mater. **2**, 338 (2003).
[24] P. Unsbo, Ph.D. thesis, Royal Institute of Technology, Stockholm, Sweden, Department of Physics, 1995.
[25] A. Jorio, R. Saito, J.H. Hafner, C.M. Lieber, M. Hunter, T. McClure, G. Dresselhaus, and M.S. Dresselhaus, Phys. Rev. Lett. **86**, 1118 (2001).
[26] P.N. D'yachkov, H. Hermann, and D.V. Kirin, Appl. Phys. Lett. **81**, 5228 (2002).
[27] A.G. Souza Filho, S.G. Chou, Ge.G. Samsonidze, G. Dresselhaus, M.S. Dresselhaus, L. An, J. Liu, A.K. Swan, M.S. Ünlü, B.B. Goldberg, A. Jorio, A. Grüneis, and R. Saito, Phys. Rev. B **69**, 115428 (2004).